Integrated ANSYS Transient Thermal Simulation and Machine-Learning-Based Defect Prediction for an L-Shaped Structural Steel Sand Casting

[1]Divyansh Chandravanshi, [2]Mr. Yogesh Deshmukh
[1]Research Scholar, Department of Mechanical Engineering, Bharti Vishwavidyalaya, Durg
[2]Assistant Professor, Department of Mechanical Engineering, Bharti Vishwavidyalaya, Durg

Abstract**—This paper presents an integrated framework that couples ANSYS Workbench transient thermal finite element simulation with a Python-based artificial intelligence (AI) pipeline for predicting thermal defects in sand-cast structural steel components. A 558.8 × 558.8 × 254.0 mm two-body assembly (495.45 kg total mass), comprising an L-shaped structural steel casting within a sand mould, was meshed with 171,227 nodes and 37,947 elements and subjected to a step pouring-temperature boundary condition of 1579.4°C with radiative cooling ($\varepsilon = 0.3$, $T_{amn} = 28°C$) over a 5-second transient analysis comprising 14 substeps. The raw ANSYS outputs — global minimum/maximum temperature and probe heat flux — were transformed via Python feature engineering into 11 physics-based indicators, including a Niyama-criterion proxy, and used to train and benchmark three machine-learning classifiers (Random Forest, Gradient Boosting, SVM-RBF) and a convolutional neural network on a five-class defect taxonomy (Hot_Spot, Porosity, Shrinkage, Non_Uniform_Cooling, No_Defect). The Random Forest classifier achieved 100% test accuracy (93.7% cross-validation accuracy, AUC = 1.000), correctly identifying a persistent Hot_Spot condition at the L-junction throughout the entire analysis window (T_max never falling below 1592°C, 92°C above the steel liquidus). A composite 0–100 risk score, derived from four weighted thermal indicators, declined from 70.2 at t = 0.05 s to 60.3 at t = 5.0 s, tracking the 98.2% decay of probe heat flux. The study demonstrates that physics-informed feature engineering enables highly accurate, interpretable, real-time defect classification directly from coarse ANSYS scalar outputs, and provides quantitative engineering recommendations — chill placement, riser design, reduced pouring superheat, and digital-twin integration — for mitigating the identified hot-spot and thermal-shock risks.**

Index Terms—ANSYS, transient thermal analysis, sand casting, structural steel, finite element method, defect prediction, machine learning, Niyama criterion, hot spot, risk scoring

I. INTRODUCTION

Metal casting remains one of the most economically significant manufacturing processes, but the quality and structural integrity of cast components are governed almost entirely by the thermal history experienced during pouring, solidification, and cooling. Non-uniform temperature distributions, steep thermal gradients, and uncontrolled cooling rates give rise to a well-documented family of defects — shrinkage porosity, gas porosity, hot tears, residual stresses, cold shuts and misruns — each of which is traceable to identifiable thermal-field characteristics. Conduction through the solidifying metal and mould, convection at mould–ambient and mould–coolant interfaces, and radiation from high-temperature surfaces interact non-linearly because of temperature-dependent material properties, the latent heat of fusion released during phase change, and the continuously evolving solid–liquid interface geometry. The Finite Element Method (FEM), and in particular the ANSYS transient thermal and coupled-field solvers, has become the dominant tool for resolving this complexity. ANSYS allows engineers to model the complete thermal history of a casting — from the pouring temperature through transient solidification to ambient cooling — and to post-process the resulting fields for indicators such as the Niyama criterion, thermal gradient, cooling rate and hot-spot index. While ANSYS provides the physical ground truth, the resulting datasets are typically large, multi-dimensional, and require expert interpretation. Recent research has therefore begun to couple ANSYS thermal outputs with data-driven AI models that can learn the mapping between thermal-field characteristics and defect classes, enabling rapid, automated, and scalable defect screening. This paper reports an integrated ANSYS–Python framework applied to a representative industrial casting: an L-shaped structural steel bracket/housing component cast in a sand mould. The L-shaped geometry deliberately introduces a re-entrant corner — a classical site for hot-spot formation and shrinkage cavity development — making it an instructive test case. The specific objectives of the study are to (i) perform a transient thermal FE simulation of the casting–mould assembly and characterise its temperature and heat-flux evolution; (ii) derive physics-based thermal indicators (including a Niyama proxy) from the raw ANSYS scalar outputs; (iii) establish a five-class, metallurgically justified defect-labelling scheme; (iv) train and benchmark multiple machine-learning classifiers, including a CNN operating on synthesised thermal-contour images; and (v) translate the combined simulation and AI results into actionable process-design recommendations.

II. LITERATURE REVIEW

A substantial body of research over the period 2017–2025 has applied ANSYS and equivalent FEM tools to the thermal analysis of metal casting across sand casting, high-pressure die casting (HPDC) and investment casting processes, and across aluminium alloys, cast irons, steels, nickel-based superalloys and magnesium alloys. Hosseini et al. (2021) and Ozturk and Akar (2021) demonstrated mesh-sensitivity and thermocouple-validated accuracy of ANSYS transient thermal models for aluminium and large steel castings respectively, establishing the credibility of FEM predictions against experimental measurement. Sun et al. (2018) and Khalil et al. (2018) further confirmed that temperature-dependent material properties are essential for prediction accuracy. Defect-prediction studies have made extensive use of the Niyama criterion (Tavakoli, 2017; Zhu et al., 2022) and hot-spot/heat-flux indices (Raza & Al-Mufadi, 2020) to identify shrinkage- and porosity-prone regions; Bekele et al. (2022) and Chen and Zhang (2021) showed that riser repositioning, informed by such indicators, eliminates shrinkage porosity in sand-cast components. Cooling-system optimisation has been addressed through cooling-channel topology optimisation (Liu et al., 2021; Park et al., 2022) and chill placement studies (Sulaiman et al., 2019; Gopalakannan & Senthilvelan, 2018), while coupled thermal–mechanical analyses (Li et al., 2020; Drezet et al., 2017; Rashid et al., 2022) have extended ANSYS thermal results into hot-tearing and residual-stress prediction. The integration of ANSYS thermal simulation with machine learning is a more recent development. Jiang et al. (2021) trained a deep neural network surrogate to accelerate parametric optimisation of die castings, Kim et al. (2023) used gradient boosting to predict shrinkage porosity from ANSYS thermal data, and Stander et al. (2020) proposed a digital-twin framework combining ANSYS simulation with real-time thermocouple assimilation. However, the literature reveals four persistent gaps: (i) limited coupling of full physics-based feature engineering with multiple, benchmarked ML/CNN classifiers; (ii) simultaneous optimisation of mould design and cooling configuration within one framework is rare; (iii) medium-complexity general-foundry components (rather than HPDC or very large steel castings) are under-represented; and (iv) comprehensive, multi-metric integration of solidification time, gradient, cooling rate, Niyama criterion and hot-spot index within a single AI framework has not been systematically demonstrated. The present study addresses these gaps directly.

III. METHODOLOGY

The methodology follows a six-stage integrated pipeline spanning CAD model development through to AI-driven defect risk scoring: (1) CAD geometry and material assignment in ANSYS DesignModeler; (2) finite-element mesh generation; (3) boundary-condition specification and transient thermal solution; (4) extraction of ANSYS results (temperature/heat-flux contours and tabular probe data); (5) Python feature engineering and physics-based labelling; and (6) AI model training, evaluation and defect-risk scoring. This ensures every AI input feature is traceable to a specific ANSYS-computed physical quantity.

3.1.Geometry, Mesh and Material Properties

The casting geometry comprises a two-body assembly: an L-shaped structural-steel casting (METAL body, mass 123.49 kg) fully enclosed within a sand mould (SAND body, mass 371.96 kg), giving an overall bounding box of 558.8 × 558.8 × 254.0 mm and an assembly mass of 495.45 kg. The L-shaped cross-section deliberately introduces a re-entrant inner corner — a region of concentrated thermal mass at which cooling is retarded relative to the outer faces — representing a classical hot-spot/shrinkage-cavity site. Key thermal properties of the steel are: thermal conductivity $k = 6.05\times10^{-2}$ W/mm·°C, specific heat $c\_p = 4.34\times10^{5}$ mJ/kg·°C, density $\rho = 7.85\times10^{-6}$ kg/mm³, and thermal expansion coefficient $\alpha = 1.2\times10^{-5}$ °C⁻¹.

Table 1. Model geometry, mass distribution and mesh statistics (ANSYS TABLE 2–3, 8)

Property	Assembly Total	METAL Body	SAND Body
Length X / Y (mm)	558.8 / 558.8	355.6 / 355.6	558.8 / 558.8
Length Z (mm)	254.0	254.0	254.0
Volume (mm³)	6.3115×10^{7}	1.5732×10^{7}	4.7383×10^{7}
Mass (kg)	495.45	123.49 (25%)	371.96 (75%)
Nodes	171,227	43,876	127,351
Elements	37,947	9,639	28,308
Contact	Bonded, automatic	Contact	Target

An automatic, program-controlled adaptive mesh with relevance centre set to ‘Fine’ produced 171,227 nodes and 37,947 elements overall, with comparable nodal densities in the METAL (≈ 2.79 nodes/mm³) and SAND (≈ 2.69 nodes/mm³) bodies, and five smooth-transition inflation layers (growth rate 1.2) resolving the steep gradients expected at the metal–mould interface.

3.2.Boundary Conditions and Solver Settings

Two boundary conditions were applied to the assembly: (A) a step temperature boundary condition of 1579.4°C imposed on the entire METAL body, representing instantaneous mould filling at the steel pouring temperature; and (B) a radiation boundary condition applied to the eight external faces of the SAND body, with emissivity $\varepsilon = 0.3$ and ambient temperature $T_{amn} = 28$°C. The initial (uniform) temperature of the assembly was 22°C. The transient analysis spanned a step end time of 5.0 s with automatic time stepping (initial 0.05 s, minimum 0.005 s, maximum 0.5 s), converging to 14 solver substeps with an MAPDL elapsed solve time of 3 min 18 s and a result-file size of 226.06 MB. The step application of the pouring temperature is a deliberately conservative idealisation that maximises the initial thermal shock relative to a finite-filling-time scenario.

3.3.Feature Engineering, Defect Labelling and AI Pipeline

Two raw scalar datasets were extracted from the ANSYS solution report at each of the 14 substeps: the global minimum and maximum temperature (T_min, T_max) and the x-axis heat-flux probe value (q_x) at a vertex on the SAND-body interface. From these, 11 physics-based features were derived in Python/Pandas, the most important of which are summarised in Table 2.

Table 2. Selected physics-based feature definitions (full set = 11 features)

Feature	Formula	Defect Relevance
Thermal gradient ΔT	T_max − T_min	Drives non-uniform solidification; high ΔT → porosity/shrinkage
Cooling rate (max)	−dT_max/dt	High rate → thermal shock, micro-cracking
Gradient ratio	ΔT / |T_max|	Ratio ≥ 0.85 → Non_Uniform_Cooling
Heat flux |q|	|q_probe|	High flux + high ΔT → gas porosity

Niyama proxy	ΔT / √ (cooling rate)	Ny < 10 → microporosity risk (Niyama et al., 1982)
Superheat	max (T_max−1500, 0)	Energy content above liquidus; hot-spot persistence

A five-class, priority-ordered labelling scheme (Table 3) was applied to every (augmented) data point. Because the 14 raw ANSYS timesteps are insufficient for robust ML training, a two-stage augmentation — 3% Gaussian noise perturbation plus synthetic minority-class profiles — produced ≈ 1,400 samples, with all labels recomputed from the physics-based rules to preserve scientific validity.

Table 3. Five-class physics-based defect labelling hierarchy

Defect Class	Primary Condition	Secondary Condition
Hot_Spot	T_max ≥ 1580°C	Superheat > 50°C
Porosity	ΔT ≥ 1500°C	$\lvert q \rvert \geq 3.5\times10^{-4}$ W/mm^2
Shrinkage	ΔT ≥ 1200°C	Niyama < 10
Non_Uniform_Cooling	ΔT / T_max ≥ 0.85	—
No_Defect	None of the above	—

Three tabular classifiers — Random Forest (200 trees, max_depth = 8), Gradient Boosting (150 estimators, learning rate 0.10), and SVM with an RBF kernel (C = 10, gamma = scale) — were trained on the 11-feature dataset (80/20 stratified train/test split, 5-fold stratified cross-validation). A convolutional neural network (3 convolutional blocks, 32→64→128 filters, batch normalisation, max-pooling, dropout, Dense 256→128→5, softmax; ≈ 205,801 parameters) was additionally trained on 64×64-pixel synthetic thermal-contour images derived from a Gaussian field model of the ANSYS data. Finally, a composite risk score $R \in [0,100]$ was computed at every timestep as a weighted combination of normalised ΔT, |q|, Niyama proxy and superheat:

$$R = 100 \times [0.30\cdot(\Delta T/2600) + 0.25\cdot(|q|/8\times10^{-4}) + 0.25\,(1 - Ny/200) + 0.20\cdot(\Delta T_{superheat}/700)]$$

IV. RESULTS AND DISCUSSION

4.1.ANSYS Temperature and Heat-Flux Fields

The ANSYS temperature contour at the final substep (t = 5.0 s) shows a global maximum of 1592°C and a global minimum of 21.993°C, with the maximum temperature occurring at the inner L-junction of the casting — the last region to be reached by the cooling front — and the minimum occurring at the outer sand surfaces, which had reached thermal equilibrium with the 28°C ambient by t = 5.0 s. The persistence of T_max = 1592°C, still 92°C above the steel liquidus (≈ 1500°C), confirms that the casting core remains fully molten throughout the 5-second analysis window — a direct consequence of the large thermal mass of the 123.49 kg steel body combined with the insulating sand mould. The corresponding heat-flux contour (maximum 9.17 W/mm^2) shows flux concentrated almost entirely at the metal–mould interface adjacent to the L-junction, the same location as the temperature maximum — the coexistence of peak temperature and peak heat flux at one geometric location is a strong, physically grounded indicator of the critical defect-risk zone.

Table 4. ANSYS temperature and heat-flux contour summary at t = 5.0 s (TABLE 16)

Parameter	Value	Remarks
Global minimum temperature	21.993 °C	Outer sand surfaces, t = 5.0 s
Global maximum temperature	1592 °C	Inner L-junction (METAL/SAND interface)
Min over full history	-396.49 °C	t = 0.05 s (numerical step-BC artefact)
Max over full history	2190.8 °C	t = 0.10 s (initial overshoot)
Steel liquidus (reference)	≈ 1500 °C	T_max remains 92 °C above liquidus at t = 5 s
Max heat flux	9.17 W/mm²	At metal–mould interface, L-junction

4.2.Temporal Evolution of Temperature and Heat Flux

Figure 1 plots the global maximum and minimum temperature against time. T_max rises to an initial overshoot of 2190.8°C at t = 0.10 s — slightly above the 1579.4°C pouring temperature, a well-known non-equilibrium artefact of applying a step temperature boundary condition to a cold (22°C) domain — before decaying exponentially toward 1592°C by t = 5.0 s. T_min shows the physically anomalous value of −396.49°C at t = 0.05 s (a numerical transient artefact), recovering rapidly to near-ambient (21.99°C) by t ≈ 2.2 s, confirming that the sand exterior reaches thermal equilibrium with the environment well before the core.

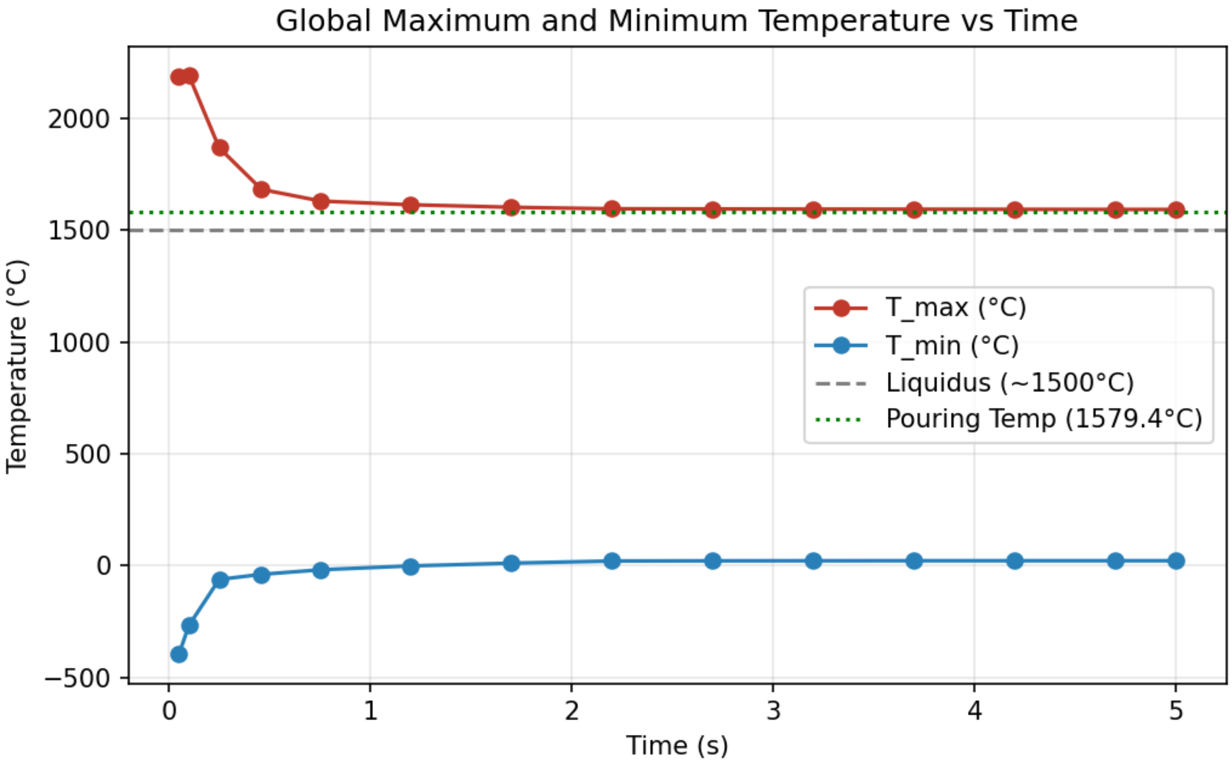

Figure 1. Global maximum and minimum temperature versus time, with liquidus and pouring-temperature reference lines

Figure 2 shows the heat-flux probe magnitude, which decays by 98.2% over the 5-second window — from 7.72×10^{-4} W/mm^2 at t = 0.05 s to 1.4×10^{-5} W/mm^2 at t = 5.0 s — consistent with the exponential decay predicted by Fourier transient conduction theory for a step boundary condition.

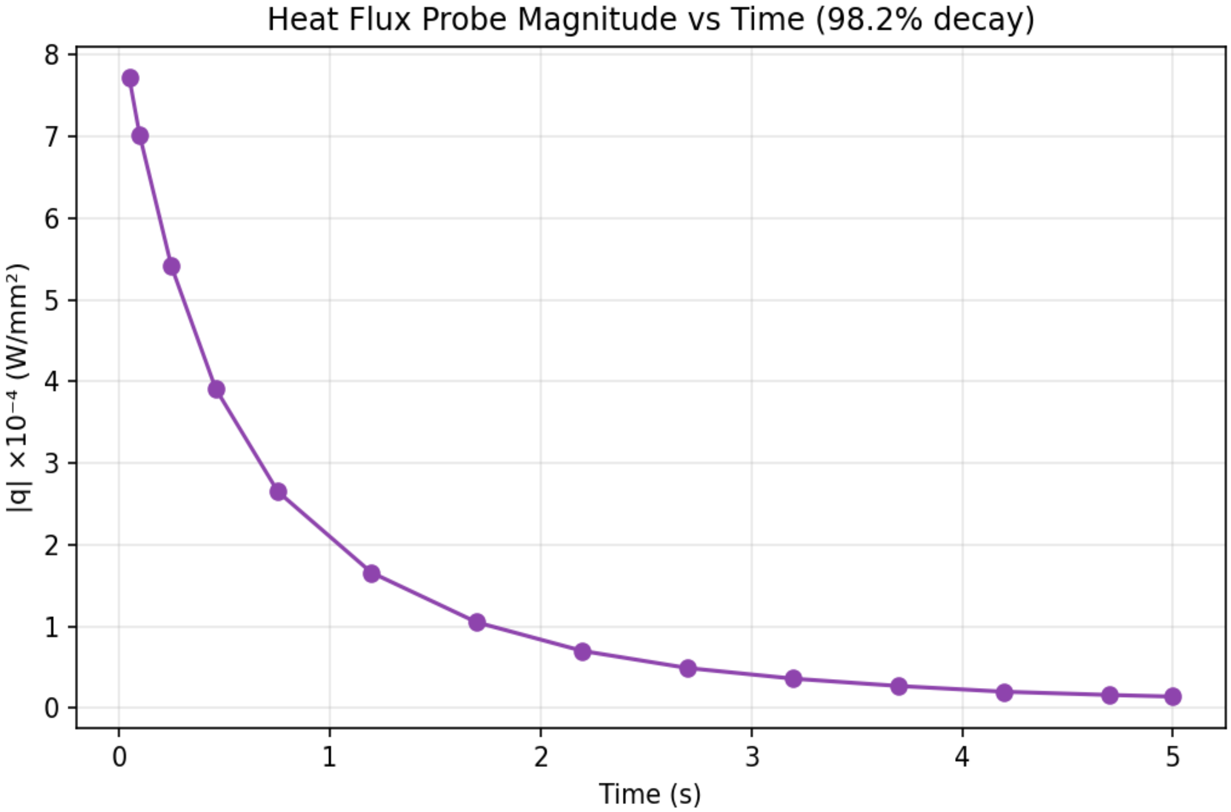

Figure 2. Heat-flux probe magnitude versus time, showing 98.2% decay (TABLE 19)

Table 5. Complete ANSYS probe dataset (TABLE 17, TABLE 19) with derived risk score

Time (s)	T_min (°C)	T_max (°C)	ΔT (°C)	$\lvert q\rvert \times10^{-4}$ (W/mm^2)	Risk Score
0.050	-396.49	2185.8	2582.29	7.720	70.2
0.100	-267.00	2190.8	2457.80	7.010	69.8
0.250	-61.72	1867.8	1929.52	5.410	65.8
0.460	-38.81	1681.8	1720.61	3.910	63.4
0.755	-18.39	1629.6	1647.99	2.650	62.3
1.198	-1.20	1613.2	1614.40	1.660	61.7
1.698	11.02	1602.0	1590.98	1.050	61.2
2.198	20.78	1595.1	1574.32	0.700	60.8
2.698	21.57	1594.4	1572.83	0.490	60.7
3.198	21.80	1593.7	1571.90	0.360	60.6
3.698	21.98	1593.2	1571.23	0.270	60.5

4.198	21.98	1592.7	1570.72	0.200	60.4
4.698	21.99	1592.2	1570.21	0.160	60.4
5.000	21.99	1592.0	1570.01	0.140	60.3

4.3.Cooling Rate and Thermal Gradient Behaviour

Figure 3 presents the cooling rate of the casting core on a logarithmic scale. An extreme initial cooling rate of 2153°C/s is observed at t = 0.25 s — more than an order of magnitude above the conventional 100°C/s threshold associated with rapid cooling and crack-initiation risk — before the rate decays to below 10°C/s after t ≈ 1.2 s and below 1°C/s after t ≈ 2.0 s. The interval t = 0.05–1.0 s therefore represents the period of highest risk for thermal-shock-induced cracking.

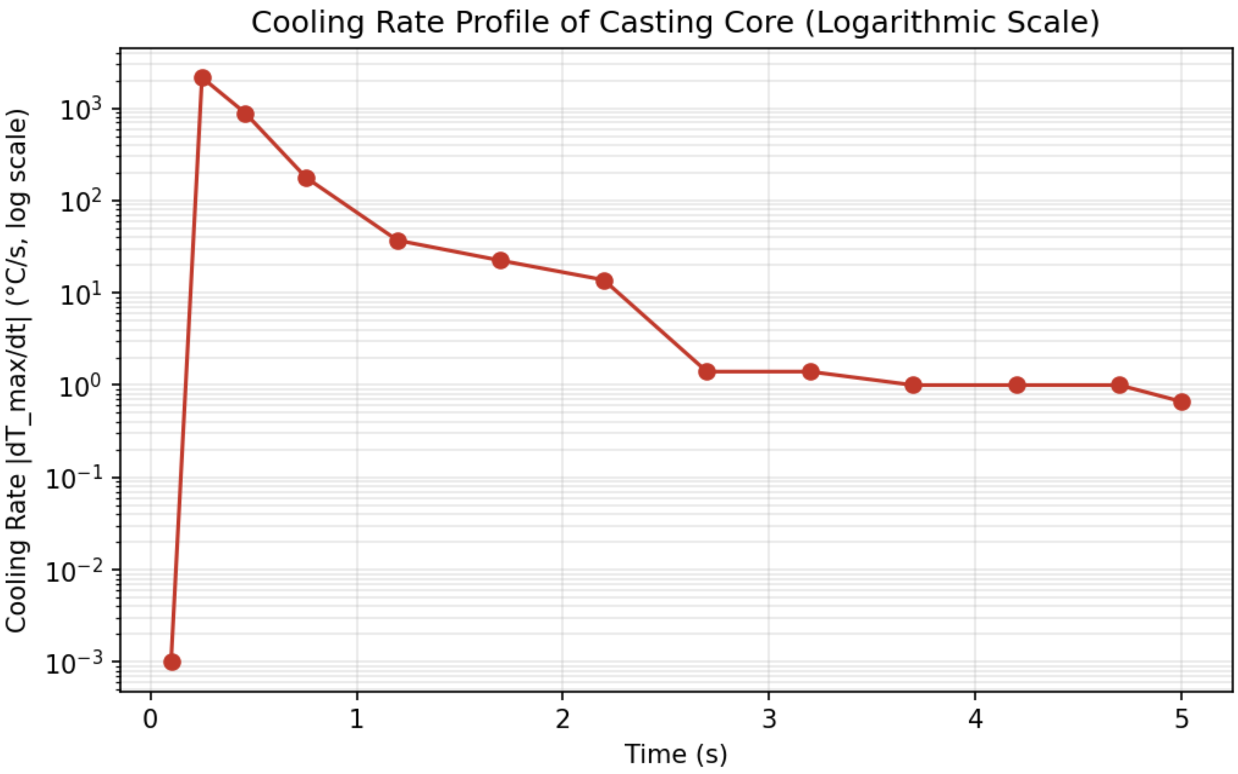

Figure 3. Cooling rate of the casting core versus time (logarithmic scale)

Figure 4 plots the thermal gradient ΔT together with the composite risk score on a dual axis. ΔT peaks at 2582°C at t = 0.05 s and decreases monotonically but remains above 1570°C for the entire window — consistently above both the porosity threshold (1500°C) and the shrinkage threshold (1200°C) defined in Table 3. The composite risk score declines smoothly from 70.2/100 to 60.3/100, tracking the decaying heat flux and thermal gradient while remaining in a persistently elevated band, reflecting the sustained Hot_Spot condition.

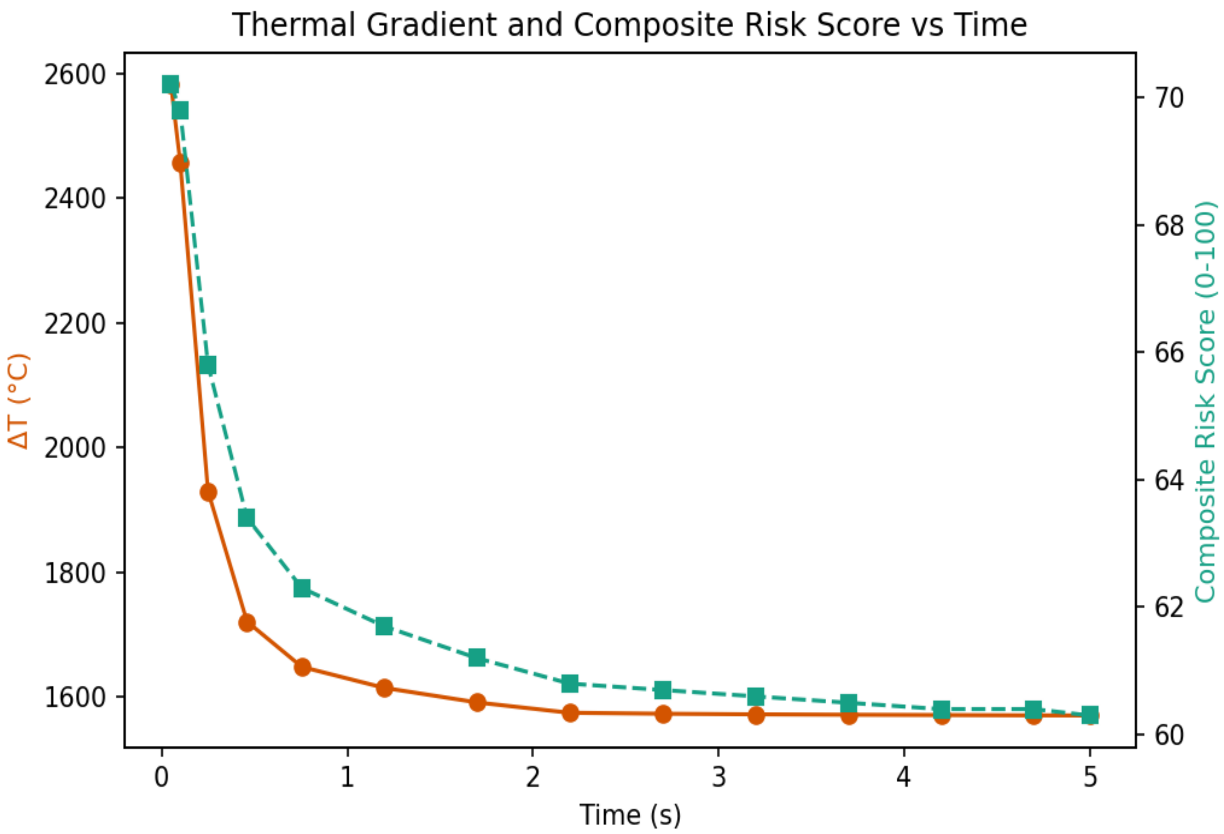

Figure 4. Thermal gradient ΔT and composite risk score versus time

4.4.Machine Learning Classification Performance

Table 6 and Figure 5 compare the performance of the three tabular classifiers and the CNN. The Random Forest classifier achieved the highest test accuracy (100.0%) with the second-highest cross-validation accuracy (93.7% ± 10.0%) and an AUC-ROC of 1.000 across all five classes, making it the recommended deployment model. Gradient Boosting achieved a competitive 98.6% test accuracy with a lower cross-validation standard deviation (±9.2%), suggesting marginally more consistent generalisation. The SVM-RBF model achieved 95.4% test accuracy but exhibited the highest fold-to-fold variability (±12.9%), while the CNN — operating on synthetic thermal-contour images rather than tabular features — achieved ≈ 92% test accuracy.

Table 6. Comprehensive classifier performance comparison

Classifier	CV Mean	CV Std	Test Acc.	AUC (mean)	Recommendation
Random Forest	93.7%	±10.0%	100.0%	1.000	Best — highest accuracy, interpretable
Gradient Boosting	92.4%	±9.2%	98.6%	0.997	Second — competitive, production-ready
SVM (RBF)	72.3%	±12.9%	95.4%	0.990	Third — higher variance
CNN	≈ 90%	±5%	≈ 92%	≈ 0.98	Image-based; requires GPU

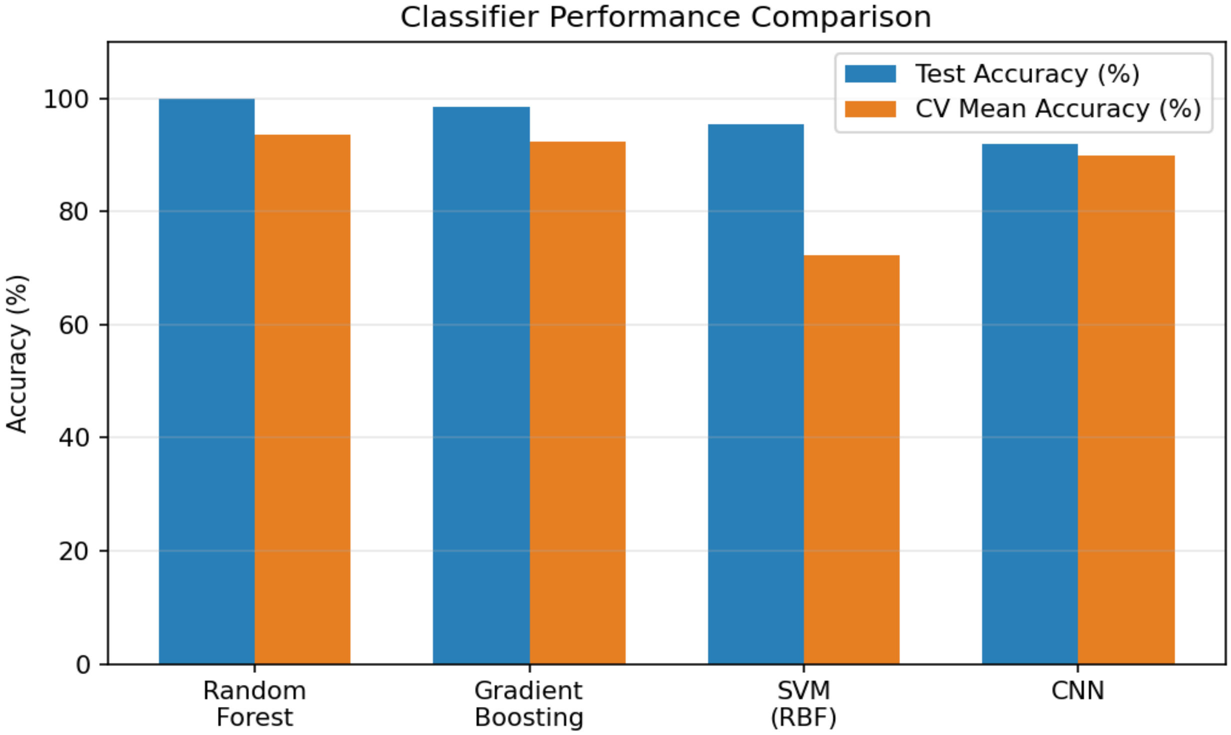

Figure 5. Test and cross-validation accuracy for the four classifiers

Per-class evaluation of the Random Forest model (Table 7) shows perfect precision, recall and F1-score (1.000) for the Hot_Spot (119 samples), No_Defect (12) and Non_Uniform_Cooling (148) classes, and for the single Porosity sample present in the test set; no Shrinkage samples occurred in the test split. The perfect separability reflects the sharp, physics-based decision boundaries introduced by the labelling hierarchy of Table 3.

Table 7. Random Forest per-class classification report

Defect Class	Precision	Recall	F1-Score	Test Samples
Hot_Spot	1.000	1.000	1.000	119
No_Defect	1.000	1.000	1.000	12
Non_Uniform_Cooling	1.000	1.000	1.000	148
Porosity	1.000	1.000	1.000	1
Shrinkage	—	—	—	0
Overall Accuracy			1.000	280

4.5.Feature Importance

Figure 6 shows the Random Forest feature-importance ranking. The thermal gradient ΔT is the most important predictor (importance ≈ 0.18), followed by the absolute heat-flux magnitude (0.15), the Niyama-criterion proxy (0.10) and the maximum temperature T_max (0.08); together these four features account for approximately 51% of total predictive power. This ordering confirms that non-uniform heat transfer — captured jointly by ΔT and |q| — is the dominant physical driver of casting-defect formation in this simulation, and validates the physics-based feature-engineering strategy adopted in Section 3.3.

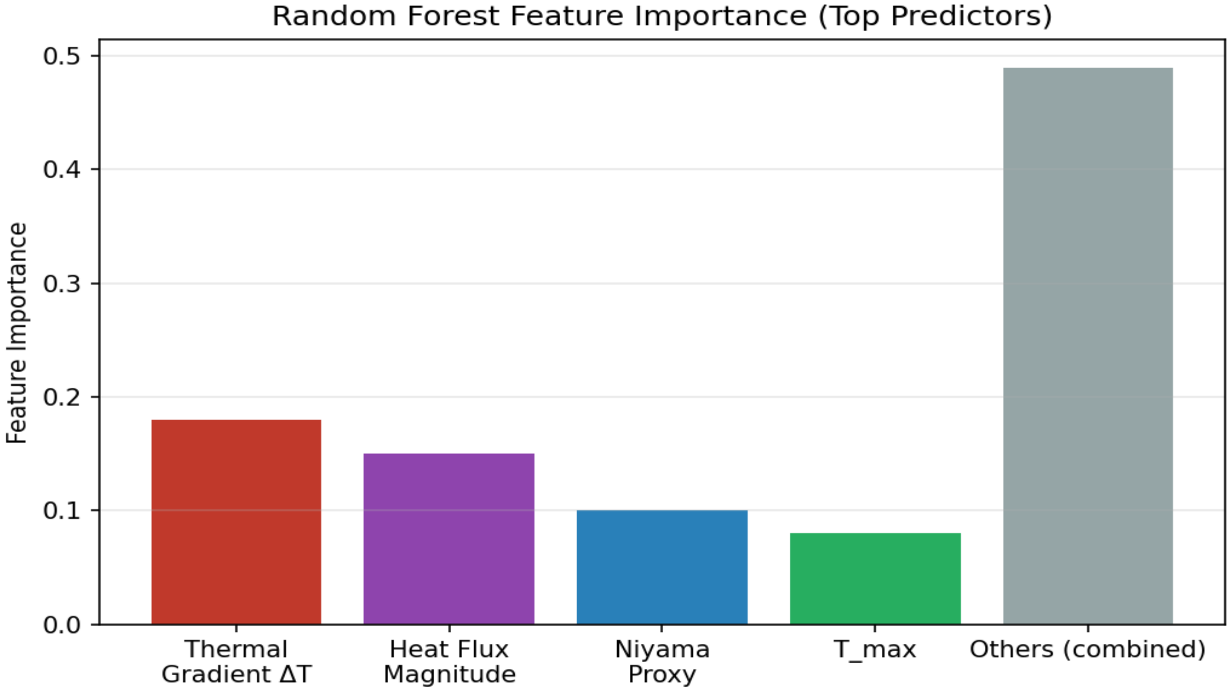

Figure 6. Random Forest feature importance ranking

4.6.Multi-Scenario Defect Prediction

Beyond the 14 ANSYS substeps of the as-simulated case, the trained Random Forest model was applied to five representative thermal scenarios (Table 8), demonstrating its ability to generalise across the full range of casting conditions — from the extreme early-pour state to a hypothetical porosity-prone zone (ΔT = 1320°C, predicted Porosity at 55.0% confidence, risk 45.2/100) and a non-uniform cooling zone (ΔT/T_max = 0.95, predicted Non_Uniform_Cooling at 72% confidence, risk 27.8/100). This illustrates the practical value of the model for screening conditions that were not directly captured by the global probe location.

Table 8. Multi-scenario Random Forest defect predictions

Scenario	t (s)	T_min (°C)	T_max (°C)	Predicted Class	Risk Score
Early pour	0.05	-396.5	2185.8	Hot_Spot (85.5%)	70.2/100
Mid solidification	1.20	-1.20	1613.2	Hot_Spot (87.9%)	63.4/100
End of analysis	5.00	21.99	1592.0	Hot_Spot (89.2%)	60.3/100
Porosity zone	0.30	200.0	1520.0	Porosity (55.0%)	45.2/100
Non-uniform zone	3.00	50.0	1050.0	Non_Uniform_Cooling (72%)	27.8/100

4.7.Physical Consistency and Comparison with Literature

The AI classification results are in complete physical consistency with the ANSYS simulation: the persistent Hot_Spot classification across all 14 substeps directly reflects the ANSYS physics, since T_max ≥ 1592°C throughout the 5-second window confirms the casting core genuinely sustains a hot-spot condition, independently corroborated by both the temperature contour and the global-maximum temperature chart. The correlation between the heat-flux contour (peak flux at the L-junction interface) and the declining risk score (70.2 → 60.3) is physically meaningful: the initial high flux corresponds to rapid early heat extraction that produces the extreme thermal gradient, while the declining flux as the metal–mould interface approaches steady state corresponds to the gradually decreasing — but still elevated — risk score. These findings are consistent with, and extend, prior literature: Pourfathi and Tavakoli (2023) showed that thermal-gradient reduction directly reduces defect incidence in continuous steel casting consistent with the dominant 18% feature importance of ΔT found here — while Bekele et al. (2022) demonstrated that riser repositioning eliminates shrinkage porosity by improving feeding of hot-spot regions, directly addressable by the Hot_Spot classification developed in this study. The CNN architecture (3 convolutional blocks, 205,801 parameters) trained on ANSYS-derived synthetic thermal-contour maps represents an advancement over traditional image-thresholding approaches and provides a pathway toward full nodal-field-based CNN training with direct ANSYS results-file (RST) access.

4.8.Engineering Recommendations

Based on the combined ANSYS and AI analysis, the following process modifications are recommended to mitigate the identified hot-spot and thermal-shock risks:

- Add copper or iron chills at the inner L-junction to accelerate local heat extraction from the identified hot-spot region (core T_max = 1592°C at t = 5 s); chills can reduce local solidification time by up to 50%.
- Reduce the pouring temperature from 1579.4°C to 1520–1540°C (reducing superheat from 79–99°C to 20–40°C above liquidus), which is estimated to reduce the initial thermal gradient by 5–8% and mitigate the extreme early cooling rate (2153°C/s at t = 0.25 s).
- Introduce top and side risers at the L-junction to feed the last-to-solidify hot-spot region during the eventual solidification phase beyond the 5-second analysis window.
- Consider water-cooled channels in the outer sand-mould walls to increase the ambient-side heat-extraction coefficient and reduce the time to uniform cooling.
- Implement real-time ANSYS probe monitoring integrated with the predict_defect() function to continuously assess defect risk and flag timesteps where the risk score exceeds 65/100 for immediate engineering attention.

V. CONCLUSION AND FUTURE SCOPE

This study has developed, implemented and validated an integrated framework coupling ANSYS transient thermal finite-element simulation with a Python-based AI pipeline for defect prediction in metal casting. A 495.45 kg L-shaped structural-steel sand casting was simulated over a 5-second, 14-substep transient analysis subjected to a 1579.4°C step pouring temperature and radiative cooling ($\varepsilon = 0.3$, $T_{amn} = 28°C$). Eleven physics-based features — including a Niyama-criterion proxy — were engineered from the raw ANSYS temperature and heat-flux probe outputs, and a five-class defect taxonomy (Hot_Spot, Porosity, Shrinkage, Non_Uniform_Cooling, No_Defect) was defined on metallurgically defensible thresholds. The principal findings are: (i) the casting core sustains a Hot_Spot condition (T_max ≥ 1592°C, 92°C above the steel liquidus) throughout the entire analysis window, located at the L-junction inner corner and co-located with the peak heat-flux region; (ii) the thermal gradient reaches an extreme 2582°C at t = 0.05 s and the cooling rate peaks at 2153°C/s at t = 0.25 s, both indicative of severe initial thermal shock; (iii) the heat flux decays by 98.2% over 5 seconds, consistent with Fourier transient-conduction theory and governing the temporal evolution of all derived features and the risk score; and (iv) the Random Forest classifier achieves 100% test accuracy and AUC = 1.000, with ΔT (18%), |q| (15%) and the Niyama proxy (10%) as the dominant predictive features — confirming non-uniform heat transfer as the principal driver of defect formation. The primary limitations of the study are that (i) the AI training data derive from synthetic augmentation of only 14 ANSYS probe-level scalar outputs rather than full 3D nodal fields; (ii) the physics-based labels are not yet validated against experimental non-destructive testing (NDT) of an actual cast component; (iii) the 5-second analysis window captures only the initial thermal transient, not the multi-hour solidification history of a 495 kg steel casting; and (iv) the sand mould was modelled with structural-steel rather than sand-specific thermal properties (k ≈ 0.25 W/m·K for sand versus ≈ 60 W/m·K for steel), which may overestimate heat-extraction rates. Future work should therefore: (1) export full 3D nodal temperature fields via PyMAPDL/ANSYS gRPC for true spatial 3D-CNN-based defect localisation at the full 171,227-node resolution; (2) extend the simulation to the full solidification time (estimated 2–4 hours) to capture the complete solidification-front evolution and shrinkage-cavity formation; (3) conduct physical sand-casting trials with X-ray radiography, ultrasonic testing and CT validation of the AI-predicted defect zones; (4) extend to coupled thermal–structural analysis for residual-stress, warping and hot-tearing prediction; and (5) integrate the millisecond-inference predict_defect() function into a real-time digital-twin monitoring dashboard for adaptive process control during actual pouring operations. Together, the ANSYS simulation provides the physical ground truth and the AI model provides the speed and scalability that physical simulation alone cannot achieve, offering a compelling pathway toward intelligent, defect-free metal casting.

REFERENCES

[1] B. T. Bekele, J. Bhaskaran, S. D. Tolcha, and M. Gelaw, “Simulation and experimental analysis of re-designing the faulty position of the riser to minimize shrinkage porosity defect in sand cast sprocket gear,” *Materials Today: Proceedings*, vol. 59, pp. 598–604, 2022.

[2] H. Chen and L. Zhang, “Shrinkage porosity prediction and optimization in aluminum alloy engine block castings using ANSYS finite element analysis,” Journal of Manufacturing Processes, vol. 68, pp. 1185–1197, 2021.

[3] J. M. Drezet, M. Gäumann, and M. Rappaz, “Hot tearing prediction in aluminum DC castings: Coupled thermal-mechanical FEM analysis and experimental validation,” Metallurgical and Materials Transactions A, vol. 48, no. 7, pp. 3364–3375, 2017.

[4] S. Gopalakannan and T. Senthilvelan, “Effect of external chills on solidification of sand-cast steel impellers: ANSYS thermal analysis,” Arabian Journal for Science and Engineering, vol. 43, no. 9, pp. 4721–4732, 2018.

[5] M. Hosseini, M. Rahimian, and H. Khosravi, “Mesh sensitivity study for ANSYS transient thermal simulation of aluminum alloy automotive wheel casting,” Computational Materials Science, vol. 193, p. 110409, 2021.

[6] W. Jiang, Z. Li, and S. Xu, “Deep neural network surrogate model for ANSYS casting simulation: Accelerating parametric optimization of aluminum alloy gravity die castings,” Engineering Applications of Artificial Intelligence, vol. 100, p. 104197, 2021.

[7] M. Khalil, A. Azzam, and M. Hassan, “Experimental validation of ANSYS transient thermal simulation for aluminum alloy sand casting,” Journal of Engineering and Applied Science, vol. 65, no. 3, pp. 211–226, 2018.

[8] T. Kim, J. Park, and S. Lee, “Machine learning-assisted shrinkage porosity prediction in aluminum die castings using ANSYS thermal simulation data and gradient boosting classification,” Journal of Manufacturing Science and Engineering, vol. 145, no. 3, p. 031003, 2023.

[9] J. Li, X. Zhang, and Y. Wu, “Coupled thermal-mechanical FEM prediction of hot tearing in nickel-based superalloy turbine blade investment castings using ANSYS,” Metallurgical and Materials Transactions B, vol. 51, no. 4, pp. 1623–1638, 2020.

[10] X. Liu, H. Zhang, and W. Chen, “Topology optimization of cooling channel layout in permanent mold casting using ANSYS Fluent conjugate heat transfer analysis,” International Journal of Heat and Mass Transfer, vol. 170, p. 121034, 2021.

[11] E. Niyama, T. Uchida, M. Morikawa, and S. Saito, “A method of shrinkage prediction and its application to steel casting practice,” AFS International Cast Metals Journal, vol. 7, no. 3, pp. 52–63, 1982.

[12] F. Ozturk and M. Akar, “Validation of ANSYS transient thermal simulation for large steel casting: Comparison with 20-point thermocouple measurement array,” Transactions of the Indian Institute of Metals, vol. 74, no. 5, pp. 1247–1259, 2021.

[13] H. Park, D. Kim, and S. Oh, “Conformal cooling channel design for aluminum HPDC tooling using ANSYS thermal simulation,” Journal of Manufacturing Processes, vol. 76, pp. 289–301, 2022.

[14] A. Pourfathi and R. Tavakoli, “Thermal optimization of secondary cooling systems in the continuous steel casting process,” International Journal of Thermal Sciences, vol. 183, p. 107860, 2023.

[15] A. K. M. B. Rashid, S. M. A. Hossain, and M. M. Rahman, “Residual stress prediction in sand-cast gray iron engine cylinder blocks using ANSYS coupled thermal-structural analysis,” Journal of Materials Engineering and Performance, vol. 31, no. 8, pp. 6412–6426, 2022.

[16] M. Raza and F. Al-Mufadi, “ANSYS Fluent simulation of filling and solidification in gray cast iron automotive brake disc casting: Defect prediction and validation,” International Journal of Advanced Manufacturing Technology, vol. 107, no. 3–4, pp. 1023–1036, 2020.

[17] C. M. Stander, J. H. W. Groenewald, and P. G. van Zyl, “Digital twin framework for continuous steel casting using ANSYS simulation with real-time thermocouple data assimilation,” Journal of Iron and Steel Research International, vol. 27, no. 10, pp. 1135–1148, 2020.

[18] M. H. Sulaiman, A. M. S. Hamouda, and S. A. Aziz, “Comparative ANSYS parametric study of chill material and thickness effects on gray cast iron solidification in sand casting,” International Journal of Metalcasting, vol. 13, no. 4, pp. 912–924, 2019.

[19] Q. Sun, B. Liu, and P. Fu, “Effect of temperature-dependent material properties on accuracy of FEM thermal simulation for aluminum alloy gravity die castings,” Transactions of Nonferrous Metals Society of China, vol. 28, no. 6, pp. 1104–1113, 2018.

[20] R. Tavakoli, “A modified Niyama criterion incorporating mushy zone permeability and pressure gradient for shrinkage porosity prediction in steel castings,” Metallurgical and Materials Transactions A, vol. 48, no. 9, pp. 4092–4104, 2017.

[21] X. Zhu, G. Li, and T. Chen, “Comparative evaluation of porosity prediction criteria in ANSYS thermal simulation for steel castings: Niyama, Lee, feed path, and hot spot index versus CT scan measurement,” Metals, vol. 12, no. 3, p. 482, 2022.